



Research papers

Upwelling processes along a western boundary current in the Abrolhos–Campos region of Brazil

A.L. Aguiar^{a,c,d,*}, M. Cirano^{c,d}, J. Pereira^{c,d}, M. Marta-Almeida^{b,d}^a Programa de Pós Graduação em Geofísica, Universidade Federal da Bahia (UFBA), Brazil^b Department of Oceanography, Texas A&M University, College Station, TX, USA^c Grupo de Oceanografia Tropical (GOAT), Instituto de Física, Universidade Federal da Bahia (UFBA), Brazil^d Rede de Modelagem e Observação Oceanográfica (REMO), Brazil

ARTICLE INFO

Article history:

Received 8 November 2012

Received in revised form

5 April 2014

Accepted 12 April 2014

Available online 4 May 2014

Keywords:

Sea surface temperature

Wind-driven circulation

Ekman transport

Ekman pumping

Brazil Current

Regional modeling

ABSTRACT

Upwelling events observed from the years 2003 to 2011 were analyzed. Our focus was on the Abrolhos–Campos region (ACR, 15°S–23°S), which is located along the Brazilian Margin and influenced by a western boundary current, the Brazil Current (BC). Satellite sea surface temperature, National Centers for Environmental Prediction (NCEP) and Global Forecast System (GFS) wind data were used to complement the results of a high-resolution regional oceanic model to investigate the occurrence of and the mechanisms responsible for intense upwelling events in this region. These events were more frequent from 20°S to 23°S. Over 90% of the identified upwelling events were influenced by favorable wind stress. Surface Ekman transport was found to be more important for the region from Prado (17°S) to Marataízes (21°S), whereas upward Ekman pumping played a more important role from 22°S to 23°S. Current-driven upwelling processes associated with the location of the BC as well as its velocity and meso-scale activity were also analyzed. The results showed that these mechanisms are highly influenced by the local topography. Topographic effects exerted via the acceleration of the BC are more obvious in the southern ACR, while in the Prado region, BC cyclonic meanders tend to be more relevant. Moreover, eddy-driven upwelling increases in the southward direction after the passage of the Vitória-Trindade Ridge (20°S), an important submarine chain, which acts to constrain and modulate the southward flow of the BC.

© 2014 Elsevier Ltd. All rights reserved.

1. Introduction

The Abrolhos–Campos region (ACR), extending from 15°S to 23°S, is a division of the Brazilian Continental Shelf adopted by Castro and Miranda (1998). It is geographically limited by the Royal-Charlotte Bank to the north and by Cabo Frio to the south and is characterized by a very complex topography (Fig. 1). In the northern part of the region, the width of the continental shelf is approximately 35 km. The shelf widens up to 190 km in the Abrolhos Bank area, and then narrows again southward, showing a width of 80 km in the Campos region, which is located between Cabo de São Tomé and Cabo Frio. The water mass structure of the upper layers results from the mixing of three water masses: (i) warm and salty Tropical Water (TW, $T > 20^\circ\text{C}$, $S > 36.40$); (ii) South Atlantic Central Water (SACW, $T < 20^\circ\text{C}$, $S < 36.40$) (Castro and Miranda, 1998), associated with the upper part of the permanent thermocline; and (iii) Coastal Water (CW), a low-salinity, high-temperature water resulting from

dilution with continental fresh water. While mixing between TW and SACW is dominant on the outer shelf, the inner shelf is filled mostly with CW near the surface (Castro and Miranda, 1998; Stramma and England, 1999).

The South Atlantic ocean circulation is highly influenced by the Subtropical Gyre. Peterson and Stramma (1991) define this gyre as follows: the Brazil Current (BC) is the southward western boundary current (WBC) that flows until the confluence with the Malvinas Current, where both currents separate from the coast and flow eastward as the South Atlantic Current. In the eastern South Atlantic, part of the South Atlantic Current turns north into the Benguela Current and finally flows into the South Equatorial Current (SEC) to close the Subtropical Gyre.

Upwelling studies classify the underlying mechanisms in two categories: wind-driven and current-driven. Wind-driven upwelling can occur due to two mechanisms: Ekman transport and Ekman pumping. The first mechanism involves water driven offshore by the alongshore component of wind stress. As a consequence, water upwells near the coast to replace the offshore Ekman transport (Smith, 1981). Under the second mechanism, in the Southern Hemisphere, a negative (positive) wind stress curl generates ocean-surface divergence (convergence), resulting in Ekman suction (pumping),

* Corresponding author at: Grupo de Oceanografia Tropical (GOAT), Instituto de Física, Universidade Federal da Bahia (UFBA), Brazil

E-mail address: alexlaguiar@yahoo.com.br (A.L. Aguiar).

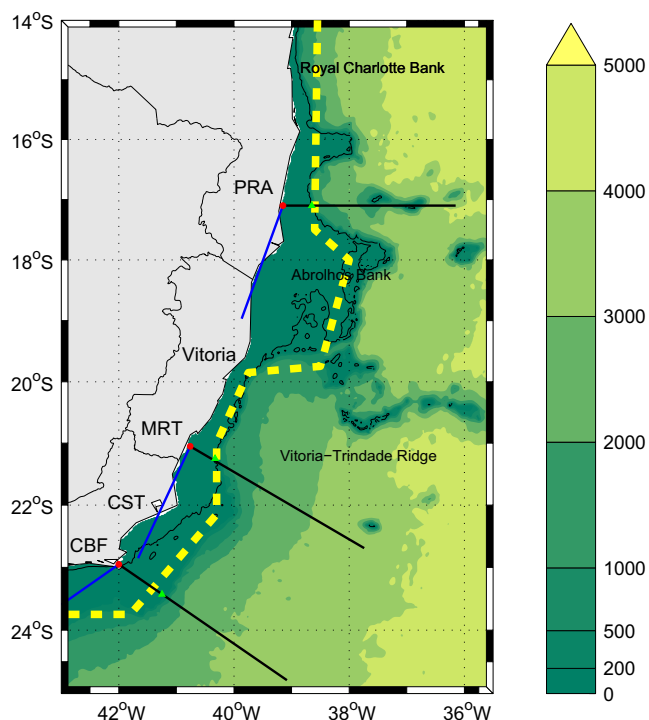


Fig. 1. Bathymetry of the study region. The 50 m isobath is represented by a light black line. The three radials (black lines perpendicular to the coastline) are used to evaluate the upwelling events. The blue lines indicate the orientation adopted to estimate Ekman transport. The red dots indicate the most onshore coastal grid point where time series of SST, wind and current velocity data were obtained. The green triangles indicate the geographical position of the shelf-break for T_{shelf} estimates. The dashed yellow line indicates the typical path of the Brazil Current. The main topographic features correspond to the Royal-Charlotte Bank, the Abrolhos Bank and the Vitória-Trindade Ridge. The abbreviations indicate the following locations: Prado (PRA), Maratáizes (MRT), Cabo de São Tomé (CST) and Cabo Frio (CBF). (For interpretation of the references to color in this figure caption, the reader is referred to the web version of this article.)

thereby forcing upward (downward) water movements (Pickett and Paduan, 2003; Castelão and Barth, 2006; Castelão, 2012). Hereafter, Ekman suction will be referred to as upward Ekman pumping.

Under the category of current-driven upwelling, a WBC can interact with the coastal system through promoting or enhancing upwelling. Current encroachment (current axis onshore movement) contributes to the pre-conditioning of the isotherms, and if the strength of the current is sufficient, enhanced Ekman transport will occur through the bottom boundary layer (BBL) (Roughan and Middleton, 2002). Separation of the current from the coast also enhances upwelling. The offshore current movement results in local divergence, causing water to outcrop toward the surface, as observed by Oke and Middleton (2001). These authors showed that cold water uplifted by the East Australian Current through bottom stress was advected by the current and outcropped to the surface further downstream in a separation zone. Furthermore, topographic variations, such as shelf narrowing/widening and changes in coastline orientation, also influence the current's dynamic features (e.g., its strength, path and meso-scale activity) and thus, current-driven upwelling processes (Lutjeharms et al., 2000; Rodrigues and Lorenzetti, 2001; Roughan and Middleton, 2002). Finally, cyclonic eddies shed by the main flow of the WBC raise the thermocline, through upward Ekman pumping due to surface divergence, to a point where the region is pre-conditioned for upwelling (Roughan and Middleton, 2002). Fig. 2 shows a schematic representation of current-driven upwelling mechanisms.

Most of the pioneering coastal upwelling studies conducted along the Brazilian coast have focused on wind-driven upwelling due to

Ekman transport (Allard, 1955; Emilson, 1961; Ikeda, 1974). These studies have shown that during spring and summer, there is a significant correlation between cold sea surface temperature (SST) anomalies and upwelling favorable northeasterly winds. Under a persistent northeasterly wind regime, SACW can outcrop to the inner shelf and sometimes reach the surface. During winter, however, these occurrences are often interrupted by the more frequent passage of cold front systems that propagate northward (Stech and Lorenzetti, 1992).

Studies focusing on other upwelling mechanisms along the Brazilian coastline have only been conducted recently and are scarce in the literature. According to Rodrigues and Lorenzetti (2001), who studied southeastern Brazilian coastal upwelling, the effects of topography and coastal geometry imply a significant influence on the upwelling process. Based on 3 numerical experiments run under different conditions (i – real topography and coastline, ii – flat bottom and real coastline and iii – real topography and smoothed coastline) with constant winds, the authors showed that variations in the alongshore bottom topography and changes in coastline geometry appear to be responsible for the location and magnitude of the upwelling cells in the region. While the intense upwelling observed in Cabo Frio is due to coastline irregularities, alongshore topographic variations have been found to be dominant over the coastline geometry in inducing upwelling from Cabo São Tomé to Vitória.

Castelão and Barth (2006) have pointed to another important wind-driven upwelling mechanism along the Brazilian coast: upward Ekman pumping. In this process, a negative wind stress curl generates ocean-surface divergence, forcing upward water movements. Their results show that the region from Vitória (20°S) to Ilha de São Sebastião (24°S) is characterized by a negative wind stress curl field throughout the year, while in the regions north of Vitória, a weak wind stress curl is found during all seasons. The maximum negative curl values are observed in summer, while the minimum values occur during autumn. The authors showed that Ekman transport and upward Ekman pumping exhibit a similar magnitude during summer. Moreover, the Ekman transport estimates for summer are relatively uniform along the coast, whereas upward Ekman pumping is strongly enhanced between 20°S and 24°S in this season. The authors suggest that wind stress curl-driven upwelling is a significant contributor to the coldest water found in the region. Castelão (2012) performed independent empirical orthogonal function (EOF) decomposition of wind stress curl and crosswind SST gradients in Cabo Frio and revealed that the patterns of variability in the fields were very similar. In addition, the spatial cross-correlations between the EOFs showed values of approximately 0.6, while the correlation coefficients between the amplitude time series of the wind stress curl and crosswind SST gradient EOFs were greater than 0.7.

Studies by Campos et al. (2000), Castelão et al. (2004) and Calado et al. (2010) have demonstrated the relevant role of BC cyclonic meanders and eddies in the current-driven upwelling process along the Brazilian Margin. These BC meanders can turn into eddies and be absorbed or released from the current. In the ACR (Fig. 1), frequent meander/eddy formation sites include the Royal Charlotte Bank (16°S), the Abrolhos Bank (18°S), Vitória (20°S), Cabo de São Tomé (22°S) and Cabo Frio (23°S) (Campos et al., 1995; Schmid et al., 1995; Soutelino et al., 2011).

With the aim of investigating the role of a cyclonic meander/eddy in the upwelling process, Calado et al. (2010) ran a 30-day Princeton Ocean Model simulation without imposing any wind forcing. By doing so, the authors were able to demonstrate the growth of a BC meander as well as the associated upwelling intensification that occurs around Cabo de São Tomé. The numerical experiment performed by these researchers provided evidence that it is possible for eddy-driven upwelling to occur in the region in the total absence of winds.

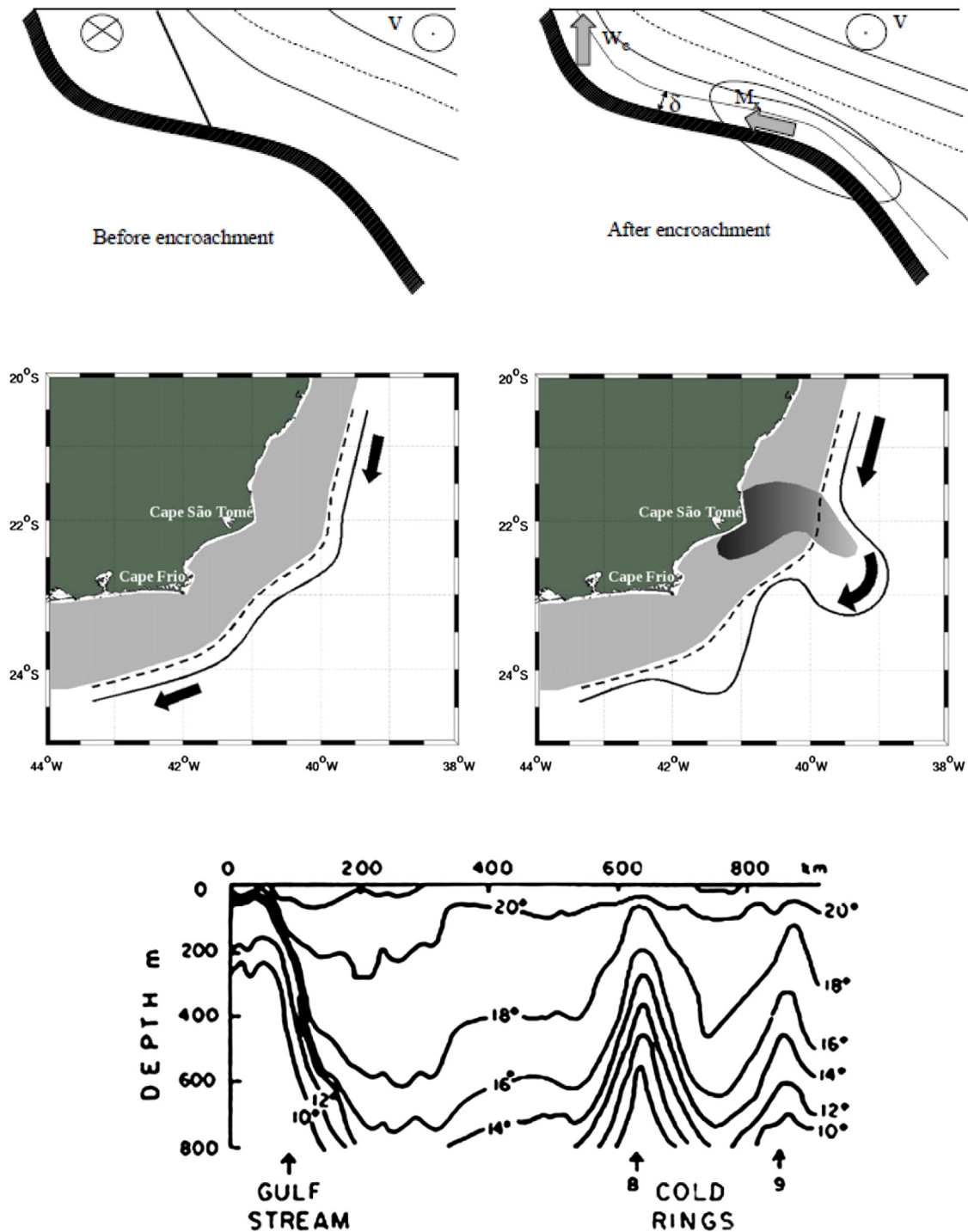


Fig. 2. Schematic representation of current-driven upwelling mechanisms. Upper panels: Before (left) and after (right) the encroachment of the current on the coast. The solid lines represent the isotachs of the southward current; the thick line represents zero velocity; and the dashed line represents the 1 ms^{-1} isotach. In the figure on the right, the oval indicates a region of high bottom stress. The alongshore current (V), mass transport through the BBL with a thickness of δ and the resultant current-driven uplift (W_c) are also shown. Extracted from [Roughan and Middleton \(2004\)](#). Middle panels: An unstable cyclonic meander of the Brazil Current (BC) growing toward the open ocean and inducing coastal upwelling. The dashed line represents the position of the shelf-break; the solid line indicates the BC front; the light gray area represents the shelf water; and the dark gray area represents the upwelled central water. Extracted from [Calado et al. \(2010\)](#). Lower panel: Vertical temperature section showing the Gulf Stream and the upward movement of its cold ring inducing water. Extracted from [Richardson et al. \(1978\)](#).

Although some knowledge of the ACR upwelling process has been amassed, most of the relevant studies were based on short-term simulations (e.g., those run for 5 days by [Rodrigues and Lorenzetti \(2001\)](#), 60 days by [Castelão et al. \(2004\)](#), and 30 days by [Calado et al. \(2010\)](#)). In the present study, upwelling events observed from the years 2003 to 2011 were analyzed. SST, National Centers for Environmental Prediction (NCEP) and

Global Forecast System (GFS) wind data, complemented by the results of a high-resolution long-term regional oceanic model simulation configured with realistic forcings (6-hourly winds, heat and freshwater fluxes via bulk formulation, large-scale oceanic forcing and tides), are used to investigate the occurrence of and the mechanisms responsible for these events in the study region.

The paper is organized as follows: the data and methods are presented in [Section 2](#), where the satellite data, model setup and analysis of upwelling mechanisms are described. The model results are discussed in [Section 3](#), where the seasonal variability is presented, followed by a description of the wind-driven and current-driven upwelling mechanisms. Finally, [Section 4](#) presents an integrated discussion of the results.

2. Data and methods

2.1. Satellite data

The SST data employed in this work were generated by the Oceanographic Modeling and Observation Network (with the Portuguese acronym REMO), which is a research and development consortium involving a group of Brazilian institutions. The REMO SST fields were obtained via sub-optimal interpolation ([Barnes, 1964](#)), using AVHRR (Advanced Very High Resolution Radiometer) thermal infrared and TMI (TRMM Microwave Imager) microwave SST data ([Kummerow et al., 1998](#)). The SST fields were produced daily with a 0.05° spatial resolution (approximately 5.55 km) and geographical coverage extending from 15°W to 70°W and 15°S to 45°S ([França et al., 2013](#)). REMO is a member of the Group for High-Resolution SST (GHRSSST), which provides a new generation of global high-resolution ($< 10\text{ km}$) SST products to the operational oceanographic, meteorological, climate and general scientific communities.

2.2. Model setup

The Regional Ocean Model System (ROMS; [Shchepetkin and McWilliams, 2005](#); [Haidvogel et al., 2008](#)) is a three-dimensional, free-surface, terrain-following model that solves the Reynolds-averaged Navier–Stokes equations using hydrostatic and Boussinesq approximations. The model is highly configurable for use in realistic regional applications. The ROMS results used in this work were based on a curvilinear grid covering most of the Brazilian coast ([Fig. 3](#)). An inclination that approximately follows the coastline was adopted. A variable cross-shore grid resolution was employed, from 2 km near the coast, where higher bathymetric gradients were found, to 12 km offshore. The resolution in the alongshore direction was approximately 9 km. The vertical axis included 32 s-levels, and the bathymetry was obtained from the ETOPO1 Global Topography database, which has a resolution of 1 arc-minute.

The modeling results that served as the basis of this work were obtained in two stages: first, in a long-term spin-up simulation and second, in operational runs that followed. The spin-up comprised two phases: the first phase ran for nine years from 1st January 2000 to 1st January 2009; the second phase ran for the next six months, until 1st July 2009. In the present work, however, only the spin-up simulations from 2003 to 2009 were used in comparisons with observed SST data, which are only available beginning in 2003. The spin-up simulation produced 5-day mean outputs. The spin-up simulation was run using lateral climatological conditions from the Ocean Circulation and Climate Advanced Project (OCCAM) model, which provided the required data (momentum, temperature, salinity and free surface) for the initial conditions as well as lateral information with a $1/4^\circ \times 1/4^\circ$ horizontal resolution.

As surface conditions, the first spin-up stage used NCEP Reanalysis-2 ([Kanamitsu et al., 2002](#)) fields for wind, humidity, pressure, temperature, precipitation and radiation. The ROMS employed these data to calculate air–sea fluxes internally through bulk formulation. The resolution of these forcings was $1.8^\circ \times 1.8^\circ$ (approximately 200 km horizontal spacing), with a time interval of 6 h. A description of the first spin-up phase and its validation can be found in [Pereira et al., 2013](#). The second

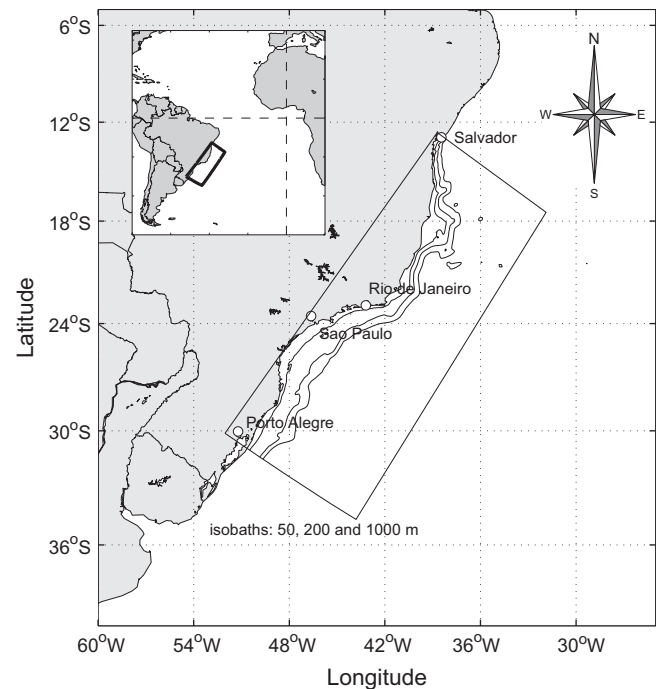


Fig. 3. Model domain. The model grid covers the Brazilian coast south of Salvador and has a variable resolution, increasing shoreward. The solid lines indicate the 50, 200 and 1000 m isobaths.

spin-up phase was an intermediate step towards operability using different atmospheric forcing. These data were provided by the GFS with a horizontal resolution of $1^\circ \times 1^\circ$ and an output sampling rate of 6 h.

Tidal forcing was used in all stages of the implementation, from the spin-up to the operational stages. The data were obtained from the TPXO 7.1 global database ([Egbert and Erofeeva, 2002](#)), which provided the amplitudes and phases of the sea surface elevation and barotropic currents for the eight primary (M_2 , S_2 , N_2 , K_2 , K_1 , O_1 , P_1 , Q_1) and the two long-period (M_f , M_m) harmonic constituents with a resolution of $1/4^\circ \times 1/4^\circ$.

The model has been operational since 1st July 2009, with spin-up phase 2 providing the initial conditions. In the operational stage, the lateral climatological forcings from OCCAM were updated to allow the $1/12^\circ \times 1/12^\circ$ horizontal resolution global oceanic model to be applied. The atmospheric forcings were also updated so that higher spatial resolution ($0.5^\circ \times 0.5^\circ$) GFS data with a more frequent time interval of 3 h could be used. The ROMS outputs were saved daily. Further details about the model configuration and the operational system can be found in [Marta-Almeida et al. \(2011\)](#).

2.3. Identification of upwelling events

Three cross-shore sections were chosen to investigate the occurrence of and the mechanisms responsible for the upwelling events observed along the ACR ([Fig. 1](#)) from the years 2003 to 2011. The northernmost section is near the city of Prado (hereafter PRA), located at 17°S , just upstream of the Abrolhos Bank. The Maratáizes section (hereafter MRT) is located at 21°S , downstream of the Vitória-Trindade Ridge. The southernmost section is Cabo Frio (hereafter CBF) at 23°S , where the coastal geometry shows a change in orientation.

Upwelling events were identified based on observed and modeled SST time series considering the most onshore coastal grid point for each section. The observed SST data were 5-day averaged to allow comparison with the modeled SST results. Due to the 5-day

temporal resolution of the employed data, the present study focus on intense, long-lived upwelling events. Furthermore, to improve spatial representativeness, an alongshore mean was also obtained for both the observed and modeled SST to expand the alongshore radius of influence to approximately 30 km. To filter seasonality and detect signals of upwelling events, the use of SST anomalies (the observed SST subtracted from its centered 90-day mean) in the upwelling analysis showed better results during sensitivity testing for the study area. To be considered an event, the observed SST anomaly had to be colder than $-1\text{ }^{\circ}\text{C}$, while the modeled SST anomaly (the modeled SST subtracted from its centered 90-day mean) was required to be at least negative. The reference value of $-1\text{ }^{\circ}\text{C}$ was adopted based on sensitivity tests and on the $-1\text{ }^{\circ}\text{C}$ intra-annual SST variability reported by Teixeira et al. (2009).

2.4. Analysis of upwelling mechanisms

To estimate the role of each upwelling mechanism in the ACR, the following upwelling indices (UIs) were established. The UIs were first classified into two categories: wind-driven and current-driven UIs (Table 1).

The wind-driven UIs were further divided into two components: Ekman transport (T_{ek}) and upward Ekman pumping (T_{pump}). The estimates of T_{ek} for the coastal grid points (in units of $\text{m}^3\text{ s}^{-1}$ per meter of coast) were obtained considering the most onshore coastal grid point and using the Smith (1968) formulation:

$$T_{ek} = \frac{\vec{\tau} \cdot \hat{t}}{\rho_o f} \quad (1)$$

where $\vec{\tau}$ is the wind stress vector; \hat{t} is a unit vector tangent to the local coastline (\hat{t} direction is indicated by the red lines in Fig. 1); ρ_o is the density of seawater (1024 kg m^{-3}); and f is the Coriolis parameter.

For the calculation of T_{pump} , the upward Ekman pumping velocity (w ; m s^{-1}) was estimated from Smith (1968):

$$w = \hat{k} \cdot \nabla \times \frac{\vec{\tau}}{\rho_o f} \quad (2)$$

where \hat{k} is a unit vector in the local vertical direction.

Thus, to compare the wind-driven UI values, the upward Ekman pumping velocity was integrated along the cross-shore axis to a distance of 200 km offshore (approximately the distance to which the negative wind stress curl extends). A similar methodology was adopted by Castelão and Barth (2006). Positive values for wind-driven UI are considered favorable for upwelling.

Concerning current-driven upwelling in the ACR region, three upwelling mechanisms were considered: BC encroachment, cyclonic meanders/eddies and topographic variations. BC encroachment is based on bottom Ekman transport through the BBL in response to the acceleration of the coastal currents and resulting bottom stress. However, the cyclonic meander/eddy mechanism is based on the dynamics of mesoscale meanders/eddies, which drive the upward movement of deep waters. Finally, topographic effects on upwelling are based on both variations in the alongshore bottom topography and changes in coastline orientation.

Thus, five current-driven UIs were established to estimate the role of each of the mechanisms cited above: BC intensification (BC_{intens}) and the proximity of the BC to the coast (BC_{prox}) associated with the BC encroachment mechanism; BC separation (BC_{sep}) and the presence of a cyclonic eddy ($Eddy_c$), associated with the cyclonic meander/eddy mechanism; and T_{shelf} , which indicates the occurrence of shelf-break upwelling, as shown in Table 1. The implications of topographic variations in relation to promoting upwelling were evaluated through comparative analysis of the events that occurred in each of the three sections.

Table 1

Wind-driven and current-driven upwelling indices.

Wind-driven UI	Current-driven UI
Ekman transport (T_{ek})	BC intensification (BC_{intens}) BC proximity (BC_{prox}) BC separation (BC_{sep})
Ekman pumping (T_{pump})	Shelf-break upwelling (T_{shelf}) Cyclonic eddy ($Eddy_c$)

It is well defined in the literature that the core of the BC is generally found at the surface, such that approximately 50% of its transport is within the first 200 m of the water column (Silveira et al., 2000). Thus, the estimates of BC behavior concerning the BC_{intens} , BC_{prox} and BC_{sep} UIs were based on the maximum southward velocity in the model s-level at the surface. BC core velocities that were more intense than the associated centered 90-day running mean were considered to represent an intensification of the BC, hence favoring upwelling. BC axial lateral movements were estimated based on the distance from core of the current compared to its average position calculated for the entire time series. Thus, positive (negative) values imply offshore (onshore) movement of the BC axis. Proximity of the BC to the coast (separation from the coast) is defined as occurring when the onshore (offshore) axial lateral movement is greater than its centered 90-day running mean. According to Oke and Middleton (2001) and Roughan and Middleton (2002), these two scenarios are favorable for upwelling.

Roughan and Middleton (2002) indicated that when moving offshore, the WBC leaves the continental shelf, flowing offshore within the subtropical gyre. However, this situation does not take place in the ACR because the BC leaves the coast farther south. In fact, the BC_{sep} UI indicates whether the BC is meandering or not (e.g., in a similar manner to the Kuroshio Current axial oscillations described by Kobayashi and Fujiwara (2009) and the BC cyclonic meanders described by Calado et al. (2010) and Palóczy et al. (2013)). As the current core moves offshore, coastal water is advected, inducing divergence, which is stronger at the surface. This divergence drives the upwelling of deep shelf waters.

$Eddy_c$ indicates whether a cyclonic eddy is present or not. $Eddy_c$ is considered upwelling favorable if the presence of a cyclonic eddy is observed within a time window of 15 days prior to the event. Our choice is compatible with the time scales described in Calado et al. (2010), who used a window of up to 30 days. In our case, we consider an eddy to be any closed circulation associated with variations in sea surface height variations of greater than 0.04 m.

The presence of shelf-break upwelling is indicated by T_{shelf} . The interactions between the WBC and the coastal system may cause intrusion of slope water, followed by pre-conditioning of the water mass field on the shelf, thus enabling weak favorable winds to produce coastal upwelling (Gibbs et al., 1998; Roughan and Middleton, 2002). When the shelf-break bottom temperature (evaluated at a depth of 50 m in PRA and MRT and 150 m in CBF) is colder than its centered 90-day running mean, shelf-break upwelling is considered to occur. To evaluate whether shelf-break upwelling occurred preceding a given upwelling event, it was necessary to estimate the time lag before the event for each section. This time lag is associated with the width of the shelf, where a certain onshore velocity is necessary to move the bottom shelf-break water up to the surface in the coastal region. An estimate of this onshore velocity was obtained based on the mean onshore velocities at the shelf region during the 9-year period and for the bottom part of the water column (20%) in each section. The time lag estimates were 50 days for PRA, 30 days for MRT and 35 days for CBF.

As the BC encroachment mechanism is based on bottom Ekman transport through the BBL in response to the acceleration of coastal

currents and resulting bottom stress, an influence of BC encroachment during an event was defined as occurring when both BC_{intens} and BC_{prox} were upwelling favorable during an event. Regarding the cyclonic meander/eddy mechanism, however, it was considered favorable if at least one of the UIs that causes divergence at the surface (BC_{sep} or $Eddy_c$) was favorable during an event.

3. Results and discussion

Fig. 4 presents the SST anomalies for the coastal region from 14°S to 23°S during the 2003–2011 period. A clear seasonality was captured in both the observed and modeled SST anomalies, with

cold anomalies occurring preferentially from September to March. This pattern is in good agreement with previous studies (e.g., Castro and Miranda, 1998; Rodrigues and Lorenzetti, 2001), showing that upwelling occurs during a limited period of the year. Although the time series are not sufficiently long to indicate inter-annual variability, the years 2003, 2005, 2007, 2008, and 2011 tend to show events occurring from austral spring to summer more clearly. A notable spatial variability is also observed in the ACR, with the southern portion presenting more frequent events.

After providing an overview of SST variability in the ACR, three sections were selected (Fig. 1) to investigate the occurrence of and the mechanisms responsible for these events in the ACR. The criteria adopted to define the sections were based not only on the

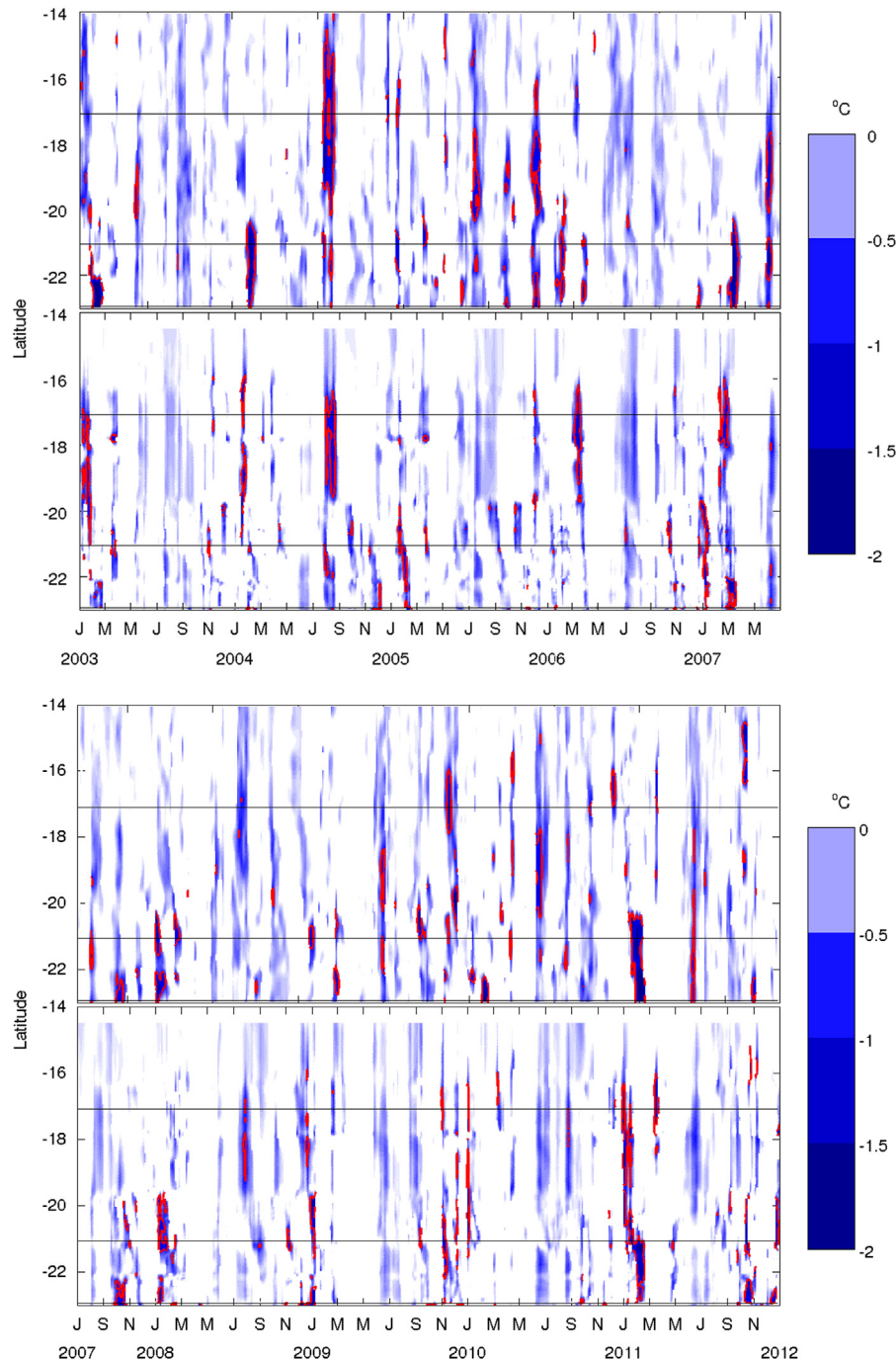


Fig. 4. Temporal variability of the observed (above) and modeled (below) SST anomaly in the coastal region from 14°S to 23°S and for the 2003–2011 period. The red isoline indicates the -1 °C isotherm. The black lines represent the location of each section (from above: PRA (17°S), MRT (21°S) and CBF (23°S)). (For interpretation of the references to color in this figure caption, the reader is referred to the web version of this article.)

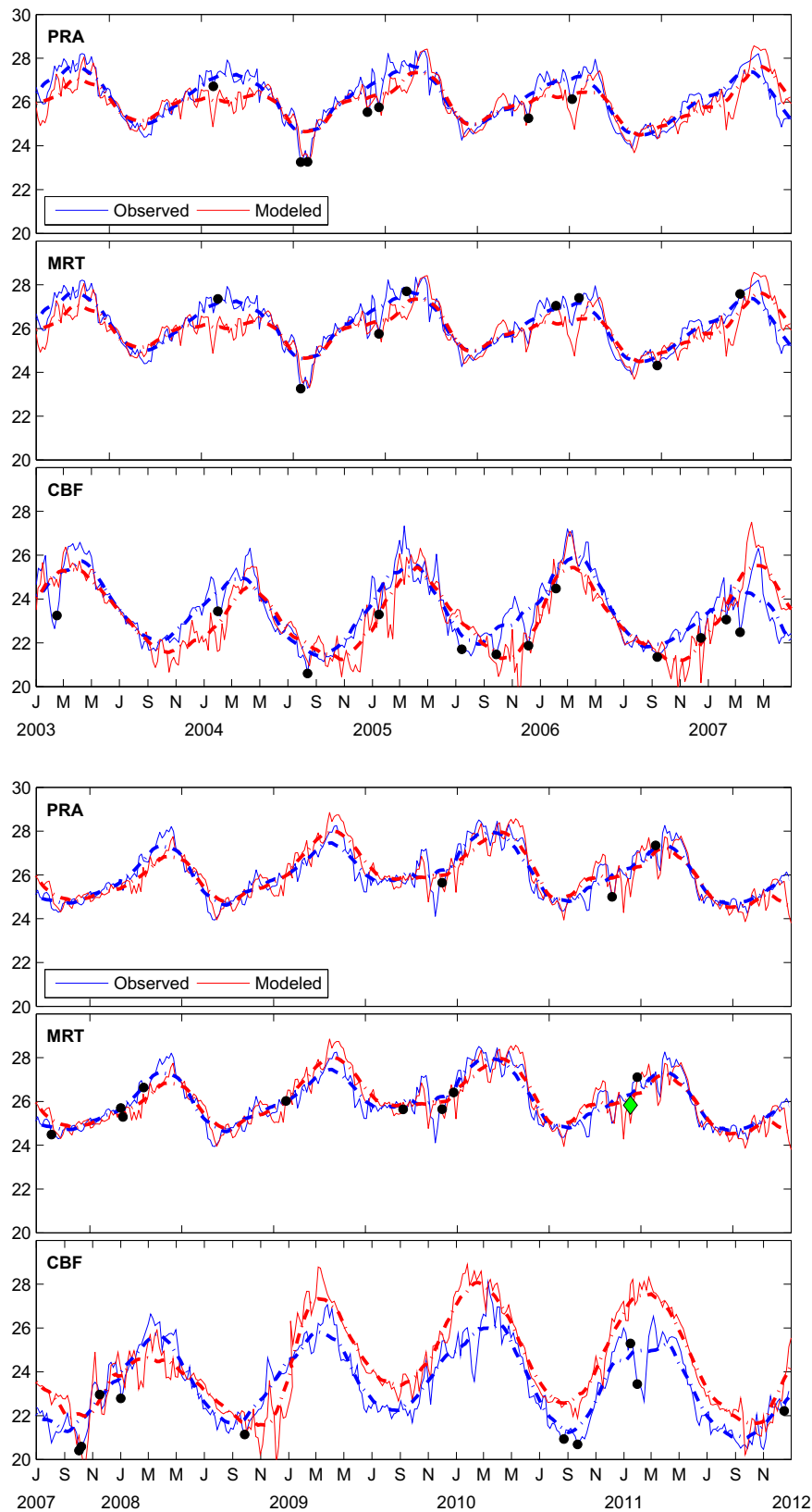


Fig. 5. Time series of the observed (blue) and modeled (red) SSTs in the coastal regions of PRA (upper panel), MRT (middle panel) and CBF (lower panel), as indicated in Fig. 1. The solid line represents the 5-day average, and the dashed line represents the 90-day running mean. Upwelling events are indicated with black circles. The case study event is indicated with a green diamond. (For interpretation of the references to color in this figure caption, the reader is referred to the web version of this article.)

number of events captured but also their intensity and the local topography to achieve a better spatial representativeness of the region. The SST time series show a well-defined seasonal pattern

for all the 3 sections (Fig. 5). In CBF, the southernmost section, a larger amplitude of the annual cycle of the SST is observed compared to the MRT and PRA sections (Table 2). These results

are in agreement with Teixeira et al. (2009). Additionally, the modeled SST compares well with the observed SST in both the spin-up run (2003–2008) and operational run (2009–2011), as shown qualitatively in Figs. 4 and 5 and quantitatively in the Taylor diagrams based on correlation values higher than 0.6 and low RMSD (root mean square deviation) values (Fig. 6). This is a good indication that the model is capable of capturing and

reproducing upwelling events and that the outputs of the two runs can be analyzed together despite their different time resolutions and forcings. The Taylor diagrams also show an increase in correlation values from the spin-up run to operational run (2009–2011), indicating that the model configuration in the operational run is more efficient than in the spin-up run (Fig. 6).

Fig. 5 shows that the number of events, defined according to the methodology presented in Section 2.4, increases southward, from 10 events in PRA to 18 events in MRT and, finally, 22 events in CBF. In PRA, the mean observed (modeled) SST during these events is 25.3 °C (25.1 °C), which decreases to 22.6 °C (22.7 °C) in MRT and reaches a minimum value of 22.2 °C (22.9 °C) in CBF. All 3 sections show values of approximately -1 °C for both the observed and modeled mean SST anomalies during the events, except in CBF, where the mean modeled SST anomaly during the events was -0.4 °C. It was demonstrated that the modelling results were poorer for CBF by the largest RMSD values obtained for this section (Fig. 6).

Table 2

Mean and standard deviation of the observed and modeled SST time series for PRA, MRT and CBF presented in Fig. 5. The units are °C.

Section	Observed SST	Modeled SST
PRA	26.1 ± 1.1	25.9 ± 1.0
MRT	23.9 ± 1.2	23.6 ± 1.3
CBF	23.5 ± 1.7	23.8 ± 2.0

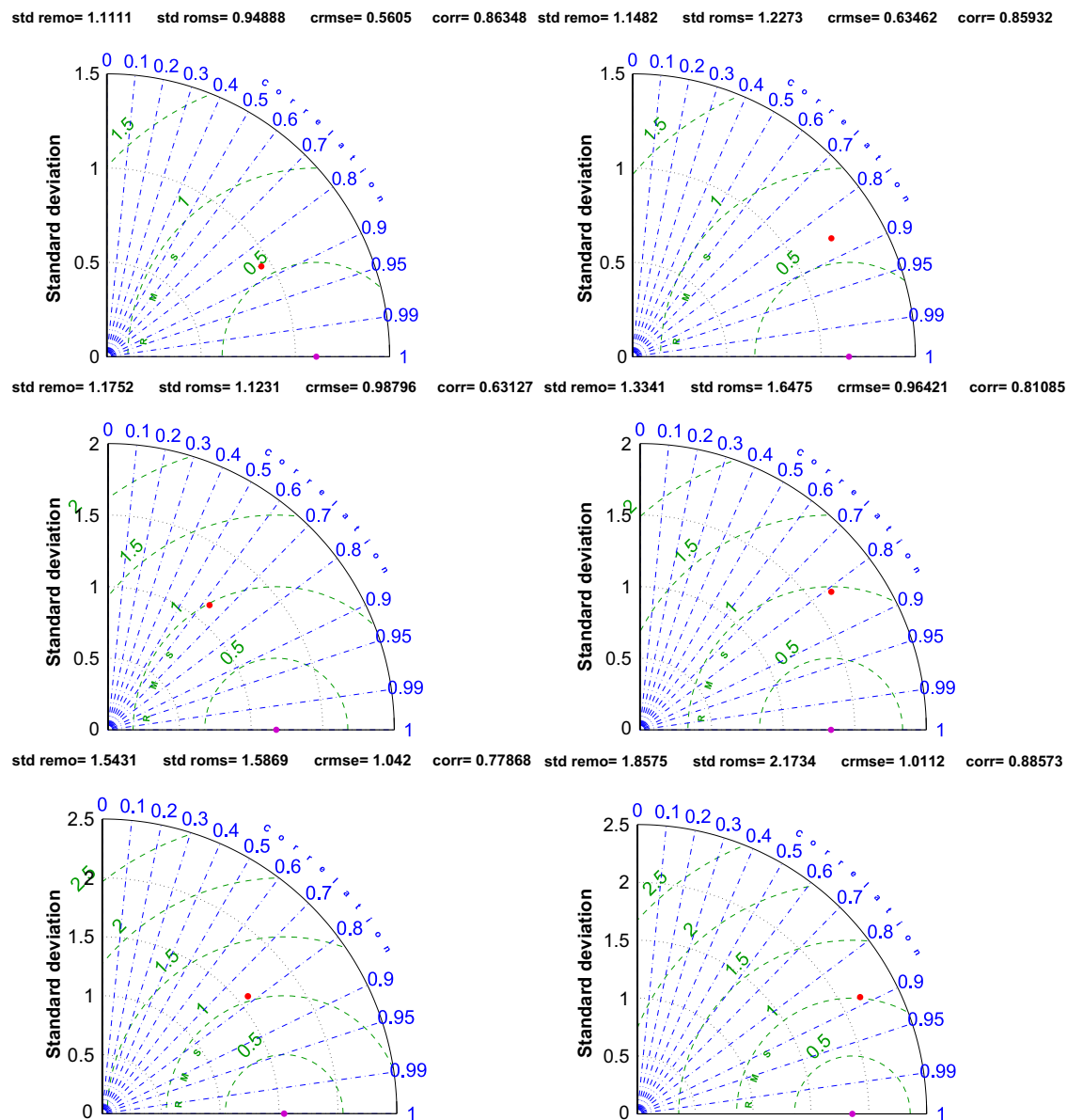


Fig. 6. Taylor diagrams for the periods from 2003–2008 (left) and 2009–2011 (right) for the PRA (upper panels), MRT (middle panels) and CBF (lower panels) sections. The purple dot on the x-axis shows where the modeled SST would fall if there was perfect agreement with the observed SST. The red dot represents the comparison of the modeled SST with the observed SST. The standard deviations of the observed (std remo) and modeled SST (std roms), root mean square deviation and correlation coefficients are indicated at the top. (For interpretation of the references to color in this figure caption, the reader is referred to the web version of this article.)

In the following two sections we use the indices defined in Section 2.4 to evaluate the contributions of wind-driven and current-driven mechanisms to the genesis of these events. In the last section, a specific event is selected and described as a case study.

3.1. Wind-driven upwelling mechanisms

The time series of the total wind-driven transport ($T_{tot} = T_{ek} + T_{pump}$) for the 3 sections (Fig. 7) show a similar seasonal pattern for the entire domain. During spring and summer (early September to late April), the T_{tot} values are greater, and most of the events occur with a positive T_{tot} , thus being upwelling favorable, in all sections. To quantify the relative importance of each wind-driven upwelling mechanism, we estimated the percentage of events that occurred when T_{tot} values and their components (T_{ek} and T_{pump}) were positive (favorable) (Fig. 8a). Additionally, the averaged transport during the events was also analyzed, as shown in Fig. 8b.

Fig. 8a shows that at least 90% of the events in PRA and CBF occurred when T_{tot} was upwelling favorable, while in MRT, all the events were influenced by T_{tot} . In PRA and MRT, T_{ek} and T_{tot} present similar percentage contributions, indicating that T_{ek} and T_{pump} work together to increase T_{tot} . In CBF, however, the percentage contribution of T_{tot} is lower than that of T_{pump} , showing that T_{ek} and T_{pump} can sometimes work in opposing ways, with the former being unfavorable and stronger than the latter during some events (Fig. 7). When T_{tot} was quantified during all the events (Fig. 8b), no significant differences were observed for the mean values among the 3 sections, which were all approximately $1 \text{ m}^2 \text{ s}^{-1}$ (Table 3). However, when these values were compared to the mean of the entire time series (Table 3), they revealed an increase of approximately 100% for all sections. However, the relative contributions of T_{ek} and T_{pump} show a different pattern during the events across the ACR. In PRA, for example, T_{ek} and T_{pump} show approximately the same mean transport during the events, presenting values of 0.47 and $0.53 \text{ m}^2 \text{ s}^{-1}$, respectively. This result is different from what has been suggested by [Castelão and Barth \(2006\)](#), who indicated that north of Vitória T_{pump} is expected to be quite small and therefore would not play a significant role in promoting upwelling. In agreement with the suggestions of these authors, it was found that in MRT, the contribution of T_{ek} is significantly larger than T_{pump} . Finally, in CBF, T_{pump} is the wind-driven upwelling mechanism with highest magnitude, presenting a value of $0.8 \text{ m}^2 \text{ s}^{-1}$.

According to the results presented above, it is evident that wind-driven upwelling mechanisms play an important role in ACR upwelling events. It is also clear that this role is performed in different ways depending on the geographical section. In MRT, the percentage of influence of T_{ek} on these events is 100%, and its average magnitude during the events is twice that of T_{pump} . Therefore, in this section, the total wind-driven upwelling is mostly due to T_{ek} . In PRA, the situation is somewhat different: T_{ek} presents a higher percentage of influence on events, but both T_{ek} and T_{pump} exhibit approximately the same intensity. In CBF, T_{pump} is qualitatively and quantitatively more important than T_{ek} and upward Ekman pumping is therefore clearly the predominant wind-driven upwelling mechanism, which is in good agreement with [Castelão and Barth \(2006\)](#).

3.2. Current-driven upwelling mechanisms

The interaction between the poleward BC and coastal upwelling along the Brazilian coast represents a challenging scenario that involves the coupling of a WBC with the associated continental shelf. Recent studies have assumed that the role of the BC in driving upwelling is more closely related to the provision of cold water in the shelf-break region. Some authors (e.g., [Campos et al.,](#)

[1995, 2000; Castelão et al., 2004](#)) claim that shelf-break upwelling is a sporadic phenomenon related to instabilities of the mean flow. Conversely, numerical experiments conducted by [Palma et al. \(2008\)](#) have shown that shelf-break upwelling extends year-round. Moreover, the results of [Palma and Matano \(2009\)](#) indicate that this persistent uplift of colder water at the shelf-break is greatly influenced by changes in pressure gradients due to variations in the alongshore bottom topography. In a recent study based on a high-density set consisting of in situ data obtained along the shelf-slope region just north of the ACR, [Amorim et al., 2012](#) discussed and expanded the role of WBCs in shelf circulation. These authors found that the presence of the Salvador Canyon (13°S), which is subject to an upwelling-favorable boundary current, enhanced the upwelling system compared to the upwelling observed on the adjacent shelf. Further south at Cabo de São Tomé (22°S), [Palóczy et al. \(2013\)](#) showed that the quasi-standing growth of a BC cyclonic meander was an effective supporting mechanism and may decrease the momentum input required from the wind to cause coastal upwelling by 50%.

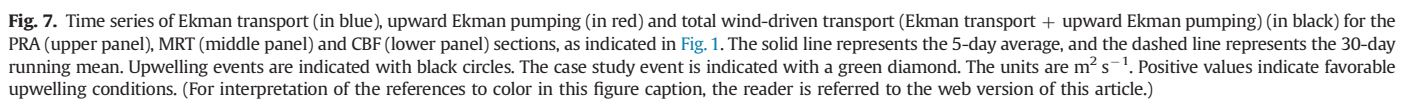
In this section, we will investigate the dynamic mechanisms of current-driven upwelling in the ACR. The UIs that capture the characteristics of the BC that are related to upwelling are described in Section 2.4 and are presented in Table 1.

Fig. 9 shows that the flow of the BC is stronger in spring and summer than in winter, which is consistent with the seasonal regime of upwelling winds. In PRA, the mean velocity of the BC is -0.19 m s^{-1} . Further south, the flow of the BC is considerably faster, reaching an average velocity of -0.56 m s^{-1} . This increase in alongshore velocity in the ACR is in good agreement with the results of [Oliveira et al. \(2009\)](#) obtained from drifting buoys, which may be because after passing through the Vitória-Trindade Ridge (Fig. 1), the BC returns to be a more stable flow in the MRT section. North of the Vitória-Trindade Ridge, [Evans and Signorini \(1985\)](#) and, more recently, [Mata et al. \(2012\)](#) reported that the larger portion of the BC turns eastward in some instances, crossing the ridge in the eastern channel and then turning back to the west, where it joins the weaker western portion further south. At other times, a large part of the BC flows through the western channel of the Vitória-Trindade Ridge ([Schmid et al., 1995](#)).

Fig. 10 shows the qualitative (favorable/unfavorable) influence of current-driven upwelling mechanisms on the events in each section. In the MRT and CBF sections, BC encroachment (favorable BC_{intens} and favorable BC_{prox}) influences approximately 30% of events, while in PRA, this influence is slightly lower (20%). These results indicate that BC encroachment cannot be considered uniform along the coast. On the contrary, depending on the location of the section, BC encroachment occurs at distinct intensities. In CBF and MRT, the average velocity of the BC increases by 10% and 20%, respectively, during upwelling events (Table 4). Moreover, the proximity of the BC to the coast is noteworthy during upwelling events in MRT, where a significant average onshore movement distance of 9.47 km is observed compared with the long-term mean position (Table 4).

The occurrence of cyclonic eddies during the identified events increases approaching the region where the coastline orientation changes (Fig. 1). The close relationship between eddy formation and the variations in the coastline orientation is well-established in the ACR ([Campos et al., 1995; Schmid et al., 1995; Soutelino, 2008; Soutelino et al., 2011](#)). In PRA, no influence of cyclonic eddies on the events was detected. In MRT, eddy-driven upwelling showed some relevance, with 2 events being influenced by a cyclonic eddy in this section. In CBF, an influence of eddies on upwelling events was observed three times more often (Fig. 10).

Fig. 11 shows that there is intense offshore movement of the BC over more than 20 km in PRA, mainly from March to July. This may be related to the seasonal variations in the position of the SEC



can be seen that the meander/eddy mechanism (favorable BC_{sep} or favorable $Eddy_c$) displays the highest percentage of influence (69%) (Fig. 10). The greatest average distance of the offshore movements

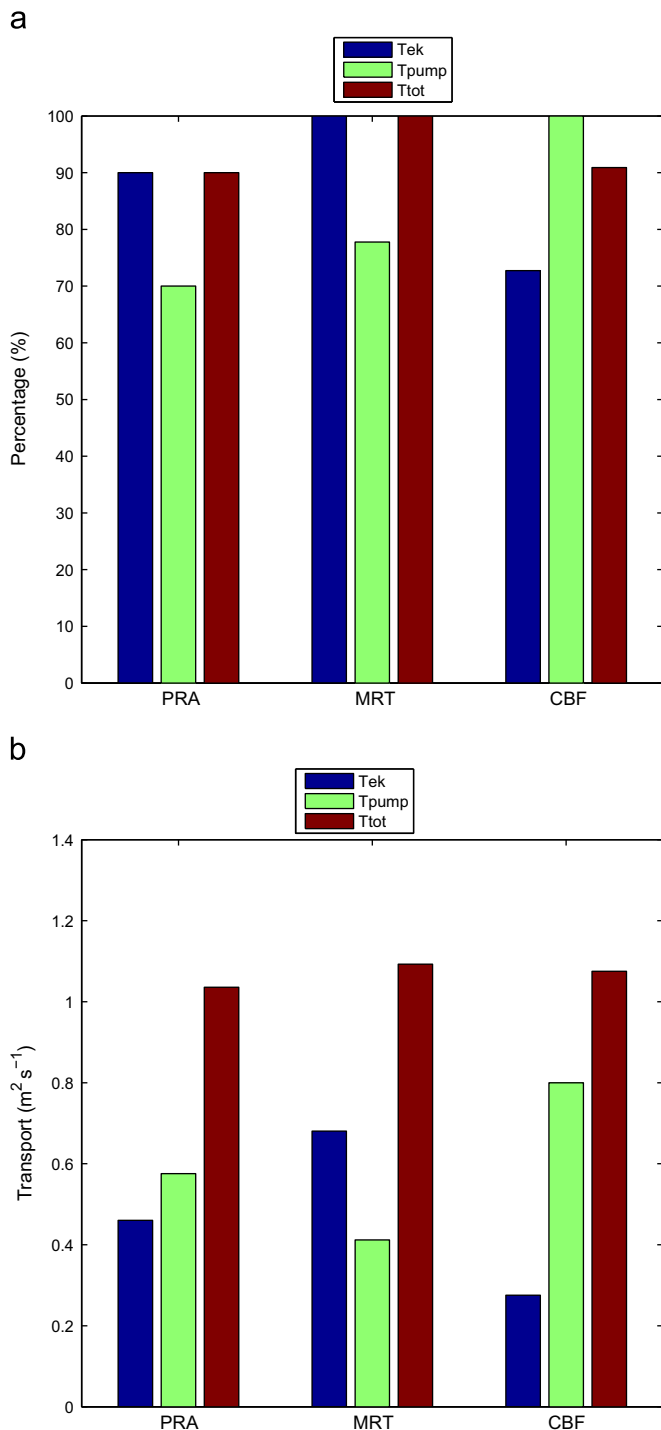


Fig. 8. Contributions of Ekman transport and upward Ekman pumping to wind-driven upwelling mechanisms: (a) percentage of influence on the events in each section and (b) average transport ($m^2 s^{-1}$) during the events in each section.

Table 3

Mean and standard deviation of the time series of T_{ek} , T_{pump} and T_{tot} for PRA, MRT and CBF presented in Fig. 7 considering the total period and only the events. The units are $m^2 s^{-1}$.

Section	Total period			Only during events		
	T_{ek}	T_{pump}	T_{tot}	T_{ek}	T_{pump}	T_{tot}
PRA	0.40 ± 0.31	0.13 ± 0.44	0.53 ± 0.67	0.47 ± 0.27	0.53 ± 0.51	1.00 ± 0.55
MRT	0.38 ± 0.41	0.20 ± 0.45	0.58 ± 0.68	0.68 ± 0.31	0.41 ± 0.68	1.09 ± 0.72
CBF	0.11 ± 0.28	0.49 ± 0.54	0.60 ± 0.69	0.28 ± 0.39	0.80 ± 0.51	1.08 ± 0.68

during events is also observed at this section, with a mean value of 7.07 km being obtained (Table 4). As no cyclonic eddies were identified during an event, BC cyclonic meanders are the main contributors to current-driven upwelling in PRA. Upwelling events in the CBF section are also influenced by the offshore movements of the BC. In 59% of the events, meander/eddy-driven upwelling takes place. However, the average offshore distance in CBF is almost halved compared to PRA, although its variability is more pronounced. Although 50% of events in MRT occur under the influence of meanders/eddy, which is a higher percentage of influence than found for BC encroachment (33%), the latter mechanism plays a quantitatively more important role in current-driven upwelling (Table 4).

The T_{shelf} UI analyzes the bottom temperature along the ACR shelf-break and the occurrence of shelf-break upwelling. The shelf-break bottom temperatures are colder towards the south (Fig. 12). In PRA, they decrease to approximately 22 °C in summer. In MRT, the presence of SACW (20 °C isotherm) can already be noted during summer, causing lower temperatures. These findings are in good agreement with Emilson (1961) concerning the occurrence of SACW along the Brazilian shelf. In CBF, shelf-break upwelling is a permanent feature throughout the year. In agreement with the previous studies conducted by Campos et al. (2000), Palma et al. (2008) and Palma and Matano (2009), our results reveal SACW outcropping to the shelf-break and inner shelf regions.

Apparently, the occurrence of upwelling events does not always correspond to shelf-break temperatures colder than the 90-day running mean. However, as the events were identified based on the SST in the coastal region, it is necessary to consider the time lag over which the shelf-break waters outcrop to the surface along the coastal region (as described in Section 2.4). For example, in CBF, during August 2004, one event was identified when T_{shelf} was warmer than the 90-day running mean. However, a colder peak was detected just before this event. According to Fig. 10, 100% of events were preceded by shelf-break upwelling in all sections. Therefore, current-driven upwelling processes are important in the ACR region in terms of preconditioning the central water mass on the shelf and shortening the response time to upwelling-favorable winds.

The results presented above show that current-driven upwelling mechanisms are relevant to understanding the upwelling processes taking place in the ACR. In summary, the intensification of the BC is stronger and more frequent during upwelling events between the MRT and CBF sections. The influence of cyclonic eddies on events increases southward due to variations in coastline geometry. Additionally, the relevance of shelf-break upwelling was indicated by the T_{shelf} UI. Shelf-break upwelling occurs mainly during summer in PRA and MRT and is more intense in the latter section, while this phenomenon is present throughout the year in CBF (persistent upwelling). Concerning the proposed current-driven upwelling mechanisms, BC encroachment (favorable BC_{intens} and favorable BC_{prox}) is predominant during events in MRT. In PRA and CBF, however, the meander/eddy mechanism (favorable BC_{sep} or favorable Eddy_c) plays a more important role during these

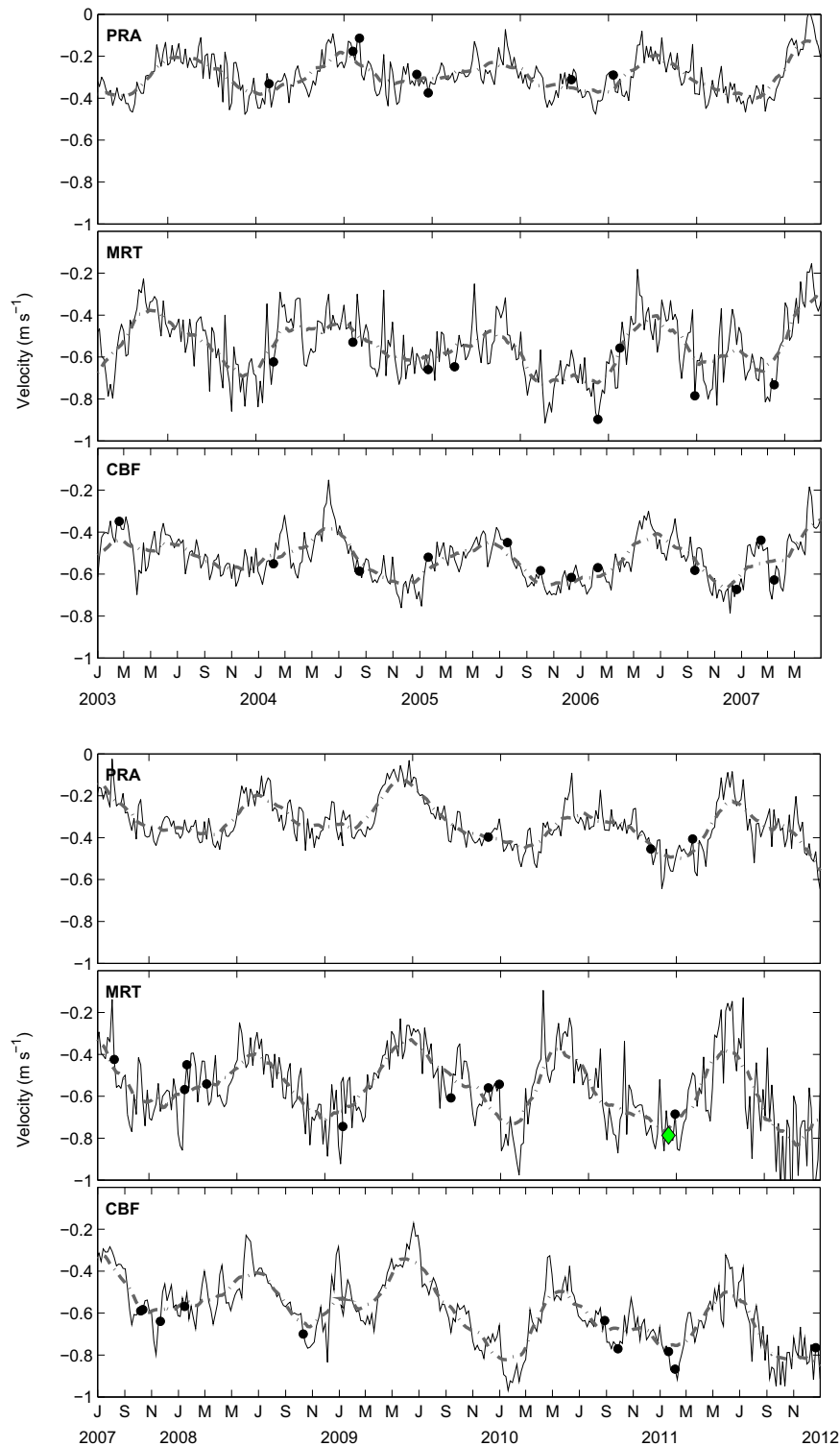


Fig. 9. Time series of the core velocity of the Brazil Current for the PRA (upper panel), MRT (middle panel) and CBF (lower panel) sections, as indicated in Fig. 1. The solid line represents the 5-day average and the dashed line represents the 90-day running mean. Upwelling events are indicated with black circles. The case study event is indicated with a green diamond. The units are m s^{-1} . (For interpretation of the references to color in this figure caption, the reader is referred to the web version of this article.)

events, despite the distance between these sections. The events in PRA are predominantly influenced only by BC meanders, whereas in CBF, both meanders and eddies are key features promoting current-driven upwelling. It can be observed that the intensity and frequency of current-driven upwelling vary depending on the section. In relation to the complex topography of the ACR, to

overcome the peculiar topographic features of the region, changes in the path, speed and meso-scale activity of the BC are observed as it flows poleward. The dynamic characteristics of the BC studied through current-driven UIs appear to be mostly determined by bottom topography. These findings agree with those reported by [Rodrigues and Lorenzetti \(2001\)](#) and [Palma and Matano \(2009\)](#).

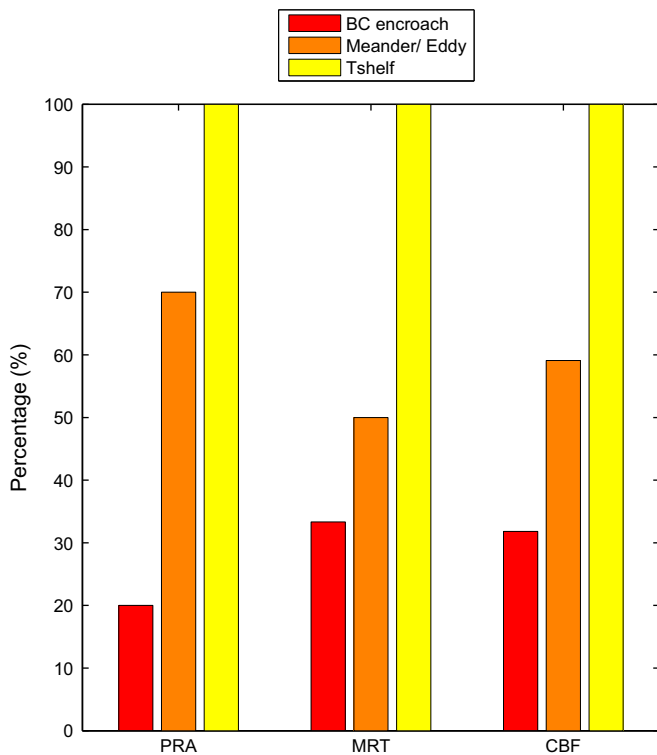


Fig. 10. Percentage of the influence of current-driven upwelling mechanisms on the upwelling events in each section.

Table 4

Mean and standard deviation of the Brazil Current (BC) core velocity and BC axial movement, where positive (negative) values indicate offshore (onshore) movement and the shelf-break bottom temperature during the upwelling events for each section according to Figs. 9, 11 and 12.

Section	Velocity (m s^{-1})	Distance (km)	T_{shelf} ($^{\circ}\text{C}$)
PRA	-0.18 ± 0.06	7.07 ± 19.33	22.1 ± 0.9
MRT	-0.63 ± 0.12	-9.47 ± 6.03	20.2 ± 1.0
CBF	-0.61 ± 0.12	3.39 ± 12.83	16.2 ± 1.2

3.3. Case study - A January 2011 MRT upwelling event

An upwelling event in MRT was chosen as a case study to obtain a better understanding of the upwelling processes off the ACR. This event was investigated in more detail in comparison with the general event analysis described above. Similarly, some of the upwelling mechanisms in the ACR were demonstrated for this particular case with the aim of understanding their roles and their effects on the coastal system. This specific upwelling event was selected among the daily outputs of the operational runs, where the date corresponds to the day when the upwelling process was strongest and most well-developed.

Fig. 13 shows that there were 3 stages (previous, intermediate and peak) of the upwelling event that occurred on the 20th of January 2011. In the previous stage, by the 31st of December 2010, pre-conditioning of the isotherms was clearly observed (Fig. 13a). As expected for the summer season, shelf-break upwelling was taking place. The 20 $^{\circ}\text{C}$ isotherm (an indication of the upper limit of SACW) reached a depth of 50 m. Divergence at the surface due to offshore currents was also observed (Fig. 13d).

During the intermediate stage (7th January 2011), the isotherms were increasingly parallel to the bottom topography as the upwelled water (SACW) occupied the inner shelf, reaching depths

shallower than 30 m (Fig. 13b). In this stage, the SACW had not yet reached the surface. Compared to the previous stage, the BC was intensified (Fig. 13e). At the surface, offshore velocities were enhanced, and a larger amount of colder shelf-break water was therefore upwelled onshore through the BBL. Near the shelf-break, velocity vectors (cross-shore/vertical) showed an upward flow starting deeper than 300 m towards the surface. The vertical advection speed of the SACW was approximately 10 m per day along the slope region. Meanwhile, a northward flow began to intensify at 39.5 $^{\circ}\text{W}$. A cyclonic eddy centered at 39 $^{\circ}\text{W}$ was observed to move toward this section. To determine whether this cyclonic eddy formed in MRT or advected from its formation site, the modeled sea surface height maps (not shown) were analyzed. The results showed that this eddy had formed in Vitória (Fig. 1) approximately one month earlier, at the beginning of December 2010. It then moved southward to MRT, after which it returned to Vitória one month later. As a consequence, there was an uplift of the isotherm in the center of the eddy at a depth of 150 m. There, the 20 $^{\circ}\text{C}$ isotherm was uplifted approximately 30 m in comparison with the previous stage, when this isotherm was flat.

Finally, on the 20th of January 2011, the SACW outcropped to the surface (Fig. 13c). A considerable offshore flow of approximately 0.2 m s^{-1} was observed at the surface at this time (Fig. 13f). In this event, T_{ek} was upwelling favorable (approximately 1 $\text{m}^2 \text{s}^{-1}$) due to the northeasterly winds blowing parallel to the coast, as seen in Figs. 7 and 14a. The wind stress curl was negative, resulting in an upwelling-favorable 0.25 $\text{m}^2 \text{s}^{-1}$ upward Ekman pumping. Thus, total wind-driven upwelling amounted to 1.25 $\text{m}^2 \text{s}^{-1}$, which is higher than the T_{tot} average value obtained during MRT events (Fig. 8b).

With regard to current-driven upwelling, the speed of the BC increased up to 0.8 m s^{-1} poleward, and BC_{intens} was favorable (Fig. 9). In comparison with the average BC core velocity recorded during events, the velocity in this case was approximately 0.15 m s^{-1} faster (25%) (Table 4). No significant axial movement of the BC was observed, and the BC core remained close to the coast, approximately in its mean position (Fig. 11). Furthermore, the cyclonic eddy became stronger (alongshore speed of approximately 0.3 m s^{-1}) and moved onshore to 39.3 $^{\circ}\text{W}$ (Figs. 13f and 14b) during the peak stage. As the eddy intensified and approached the coast, the flow of the BC appears to have been constricted and, moreover, intensified by the onshore movement of the cyclonic eddy (Fig. 13f). Another noteworthy finding was that the isotherms responded according to this eddy movement, which might have increased the availability of the SACW for upwelling near the coast (Fig. 13c). Considering these two processes, the main contributor to eddy-driven upwelling appears to have been the acceleration of the flow of the BC due to its constriction, rather than SACW pre-conditioning, as the former phenomenon occurred weakly (approximately a 30 m isotherm uplift) 50 km away from the coast. The intensification of the BC implies the existence of enhanced bottom stress in the shelf and slope region, thus increasing vertical mixing and lengthening the time it takes for the BBL to shut down (MacCready and Rhines, 1993). Hence, upwelled water was driven onto the shelf towards the surface over a longer period of time.

In this case study, it was possible to observe the evolution of the upwelling event up to its peak stage in MRT as well as the processes and forcing mechanisms involved. In this situation, the SACW outcropped to the surface. Ekman transport was the prevailing wind-driven upwelling mechanism, with upward Ekman pumping making an additional contribution. Current-driven upwelling processes also played an important role in this event. As the BC intensified, isotherms were uplifted parallel to the bottom topography. At the same time, the intensification of the BC promoted an increase in bottom stress along the shelf and

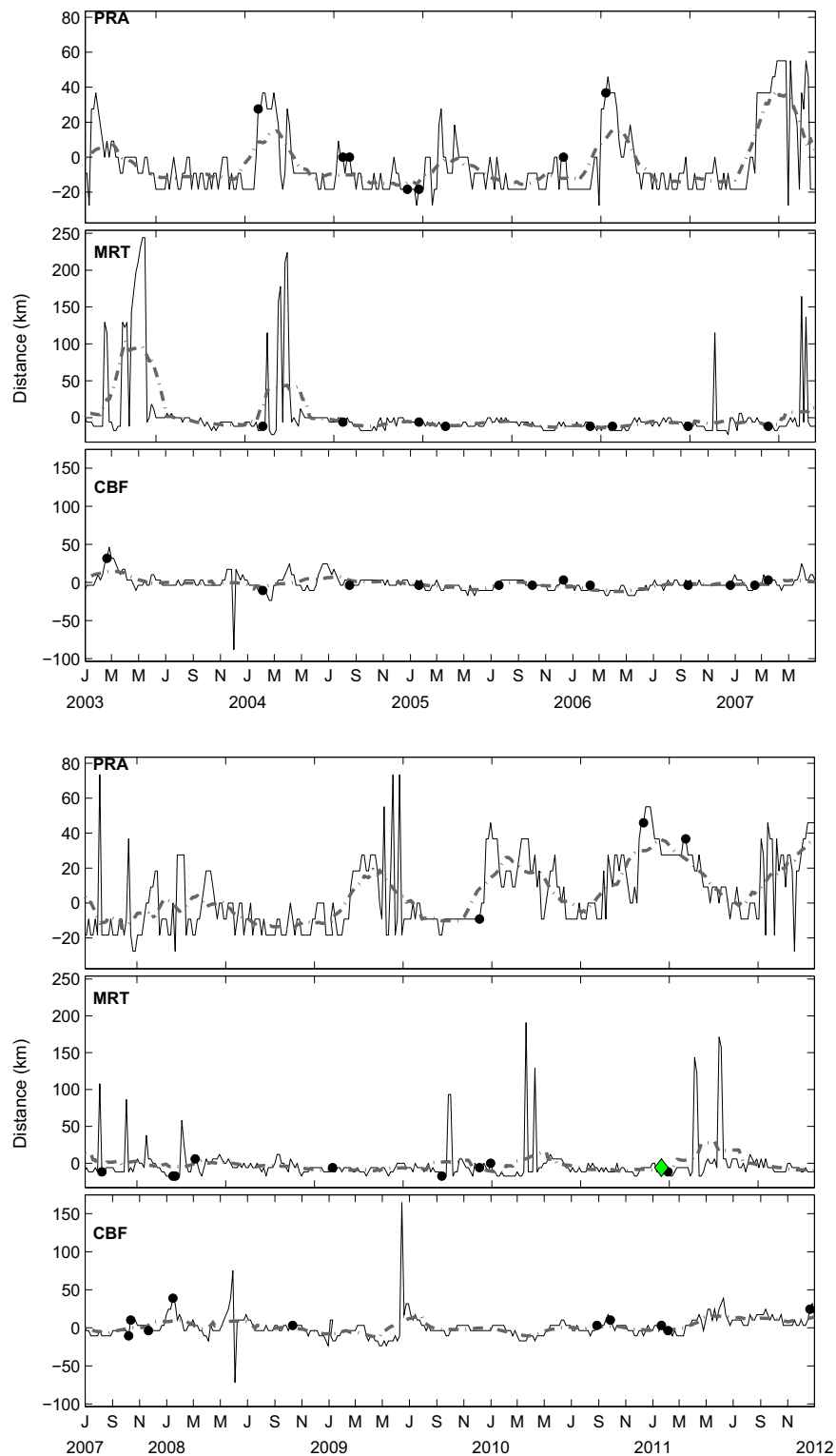


Fig. 11. Time series of the axial movement of the Brazil Current for the PRA (upper panel), MRT (middle panel) and CBF (lower panel) sections, as indicated in Fig. 1. The solid line represents the 5-day average, and the dashed line represents the 90-day running mean. Upwelling events are indicated with black circles. The case study event is indicated with a green diamond. Positive (negative) values indicate offshore (onshore) movement of the current. The units are km. (For interpretation of the references to color in this figure caption, the reader is referred to the web version of this article.)

slope region, and the BBL shutdown time was therefore lengthened. Another current-driven upwelling process observed was the cyclonic eddy effect. The growth and onshore movement of this phenomenon caused constriction and, hence, acceleration of the BC, increasing bottom stress and enhancing upward water

movements. Furthermore, uplift of SACW towards the coast to shallower depths due to the cyclonic eddy effect was also noted. As indicated in Section 3.2, these processes are strongly related to alongshore topographic variations. Therefore, this upwelling event was predominantly topographically induced.

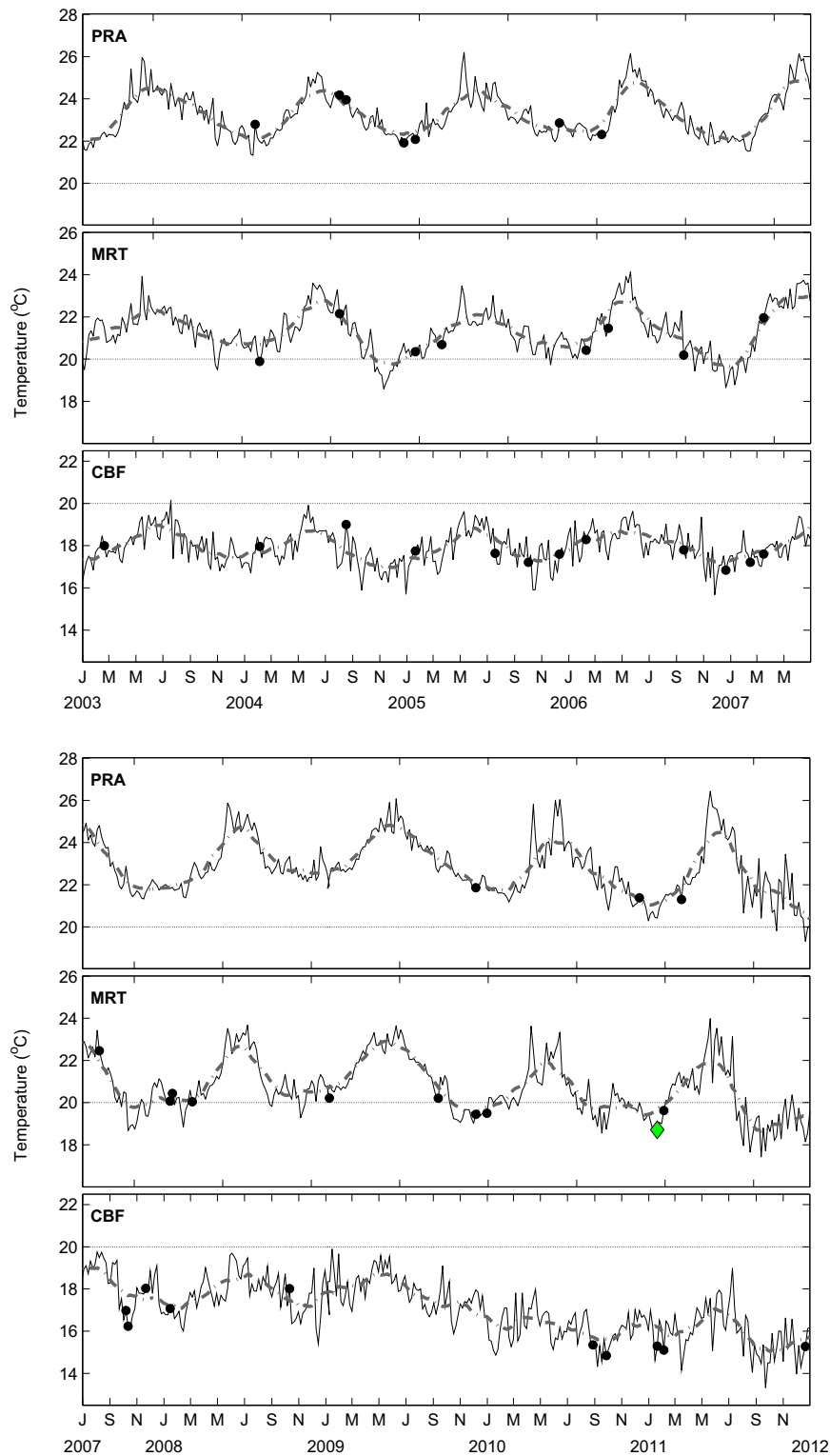


Fig. 12. Time series of the shelf-break bottom temperature for the PRA (upper panel), MRT (middle panel) and CBF (lower panel) sections, as indicated by the green triangles in Fig. 1. The solid line represents the 5-day average, and the dashed line represents the 90-day running mean. Upwelling events are indicated with black circles. The case study event is indicated with a green diamond. The units are °C. (For interpretation of the references to color in this figure caption, the reader is referred to the web version of this article.)

3.4. Limitations underlying the use of model simulations with different time resolutions and wind forcings

The ROMS is a widely employed ocean model for studying regional processes. In the present work, both spin-up and operational

simulations were used to investigate upwelling processes and mechanisms across the ACR. To capture upwelling signals and the dynamics of the underlying mechanisms, we had to address distinct temporal resolutions and wind forcings among the simulations. Although the operational runs could be performed on a daily basis,

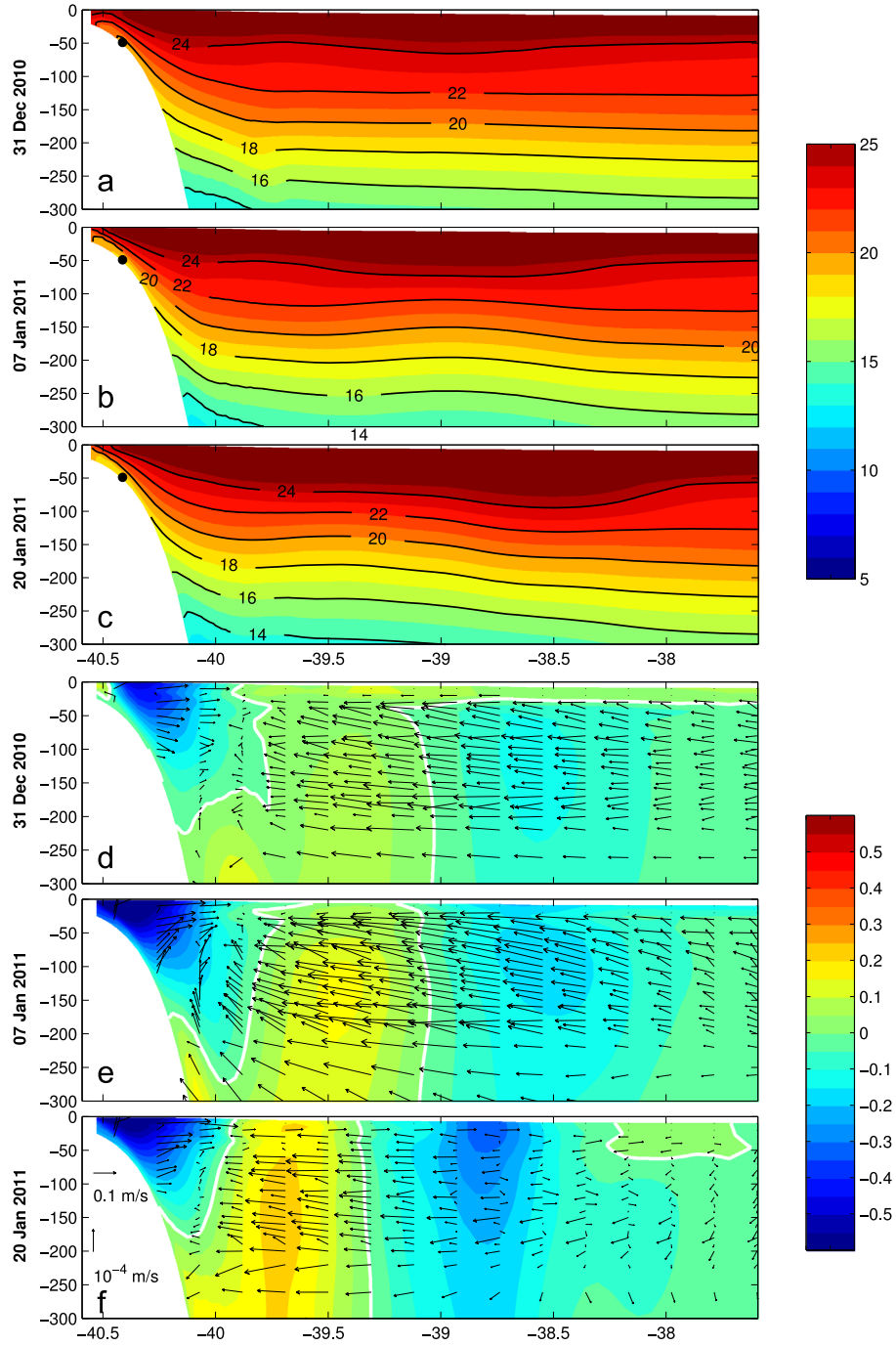


Fig. 13. Cross-shore section of temperature during the (a) previous stage, (b) intermediate stage and (c) peak stage of the case study upwelling event in the MRT section. The interval between the isotherms is 2 °C. Cross-shore section of the associated alongshore velocity in the (d) previous stage, (e) intermediate stage and (f) peak stage of the same event. Negative (positive) velocities are southward (northward). The interval between isotachs is 0.05 m s⁻¹. Vectors indicates the cross-shore/vertical velocity field. The black dots indicate the geographical position of the shelf-break for T_{shelf} estimates for this section.

and observed SSTs were available at this temporal resolution, these data were 5-day averaged to make them comparable with the spin-up outputs. We acknowledge that the decision to extend SSTs from 2003 to 2011 (nine years) led to a decrease in the power of the methods employed to identify upwelling events compared with using data only for the period from 2009 to 2011 (three years), for which the daily results are available. Thus, over the period of 9 years we were only able to identify 10–22 events. For example, using SST data from Geostationary Environmental Operational Satellites (GOES) (6 km, 1-hour resolution), Palóczy et al. (2013) identified 62 events at

Cabo de São Tomé over a similar period (from September 2003 through March 2012). However, these authors based their analyses on a simplified 2D Princeton Ocean Model (POM) experiment, which was unable to represent any particular characteristics of the time-dependent circulation. In contrast, the use of ROMS simulations in the present study allowed us to obtain more representative model results regarding time-dependent upwelling processes and the dynamics of the associated mechanisms. Still, considering the frequency of the data employed in this study, its results are restricted to intense and long-lived upwelling events.

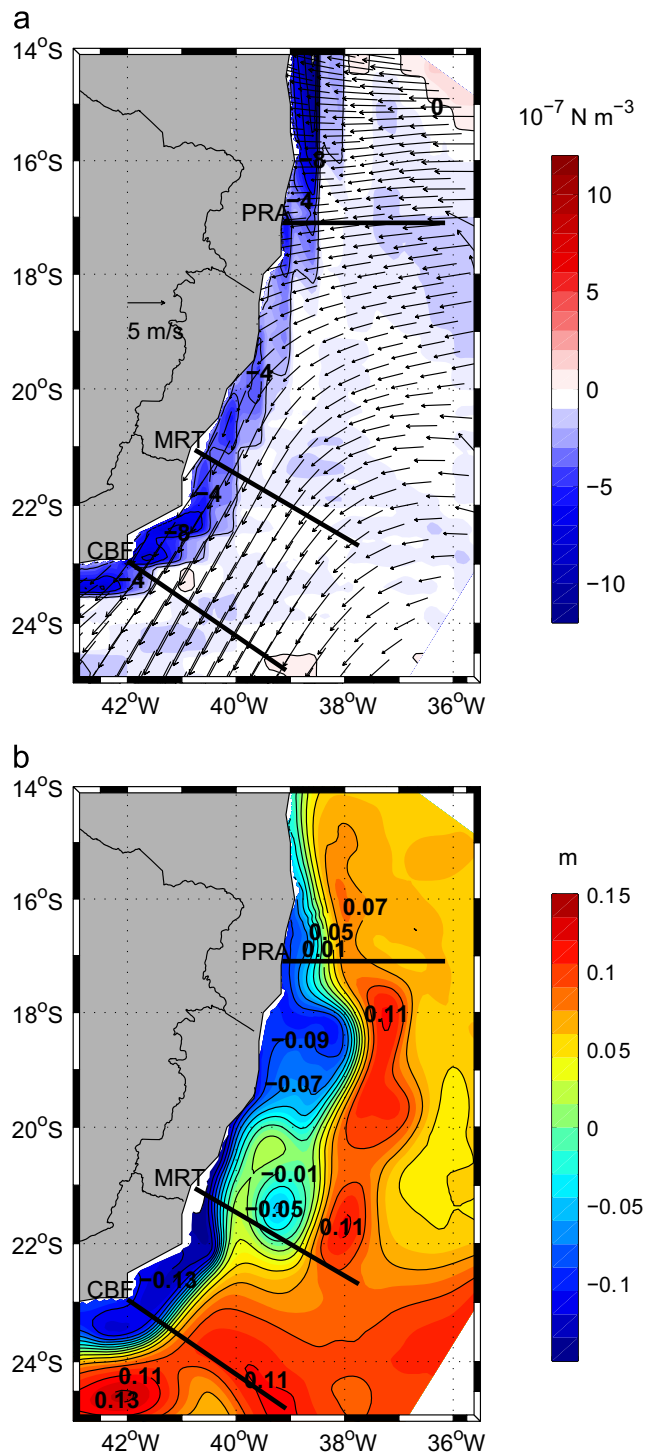


Fig. 14. (a) Wind stress curl with vectors indicating the wind field at 10 m and (b) sea surface heights during the peak stage of the case study upwelling event. The intervals between isolines are (a) $2 \times 10^{-7} \text{ N m}^{-3}$ and (b) 0.02 m.

4. Summary and conclusions

Upwelling occurs under distinct patterns and forcing mechanisms depending on where it takes place around the world. This phenomenon has remarkable importance due to its implications for ocean dynamics, petroleum exploration and fisheries production. Thus, it is necessary to understand the characteristics of upwelling phenomena as well as the associated processes involved and the mechanisms responsible for the occurrence of these events in the ACR.

Along the Brazilian margin, most studies addressing coastal upwelling in the ACR have focused on the CBF region. It is well-established that upwelling is enhanced in vicinity of CBF. Most of these previous studies have related the upwelling in this region to offshore Ekman transport (due to northeasterly winds blowing parallel to the coast). More recently, other forcing mechanisms have been considered to explain this phenomenon. The main forcings proposed to exist in the ACR, in addition to Ekman transport, are upward Ekman pumping due to the negative wind stress curl, the interaction of the BC with variations in the alongshore bottom topography and the irregularities of the coastline geometry and, finally, BC cyclonic meanders/eddies. Although significant results were obtained, most of these studies were based on short-term numerical simulations.

In this work, high-resolution satellite SST, NCEP and GFS wind data were used in conjunction with the outputs of a long run of the ROMS, covering a 9-year period (2003–2011), to study the upwelling processes off the ACR. Over time, the events exhibited clear seasonal variability, predominantly occurring during austral spring and summer. In space, the southern portion of the region was marked by more frequent and also stronger events.

The analysis of forcing mechanisms revealed that wind-driven upwelling is a very important component of the process, with Ekman transport and upward Ekman pumping acting together to promote upwelling in most of the events. While Ekman transport is the predominant forcing mechanism along the northern portion of the ACR, upward Ekman pumping tends to prevail in southern portion of this region, where changes in coastline orientation are more obvious.

As a complementary part of the process, the current-driven upwelling mechanisms are highly influenced by the local topography. Knowledge of the bottom topography and coastline geometry is critical for understanding the temporal and spatial changes in the path, velocity and meso-scale activity of the BC. The intensification of the BC was found to be important from MRT to CBF, possibly due to the influence of the Vitória-Trindade Ridge on the poleward flow of the BC. While the BC cyclonic meanders enhance upwelling in PRA and CBF, BC encroachment prevails in MRT. Eddy-driven upwelling, in turn, plays a significant role from MRT to CBF, showing a higher intensity southward approaching the region where the coastline orientation changes. Hence, in agreement with [Rodrigues and Lorenzetti \(2001\)](#) and [Palma and Matano \(2009\)](#), our results demonstrate that topographically induced upwelling plays the main role among the current-driven mechanisms in the ACR.

Finally, in the case study described in this work, an upwelling event caused by the wind, current and cyclonic eddy presence in the MRT section was evaluated, and the role played by each process was investigated. In this particular event, while Ekman transport was found to be more important than upward Ekman pumping for wind-driven upwelling, alongshore topographic variations were shown to be the prevailing mechanism impacting current-driven upwelling.

Acknowledgments

This research was supported by PETROBRAS and approved by the Brazilian oil regulatory agency ANP (Agência Nacional de Petróleo, Gás Natural e Biocombustíveis), under the special participation Oceanographic Modeling and Observation Network (REMO) research project. Mauro Cirano and Alessandro L. Aguiar were supported by a CNPq research grant and scholarship, respectively. We thank three anonymous reviewers for their thoughtful comments.

Appendix A. Supplementary data

Supplementary data associated with this article can be found in the online version at <http://dx.doi.org/10.1016/j.csr.2014.04.013>.

References

- Allard, P., 1955. Dans les températures de l'eau de mer observées au Cabo Frio Brésil. *Bull. Inf. Com. Cent. Océanogr. Études Cotes* 7 (2), 58–63.
- Amorim, F.N., Cirano, M., Soares, I.D., Campos, E.J.D., Middleton, J., 2012. The influence of large-scale circulation and transient processes on the seasonal circulation at Eastern Brazilian Shelf near 13°S. *Cont. Shelf Res.* 32, 47–61. <http://dx.doi.org/10.1016/j.csr.2011.10.011>.
- Barnes, S.L., 1964. A technique for maximizing details in numerical weather-map analysis. *J. Appl. Meteor.* 3 (4), 396–409.
- Calado, L., da Silveira, I.C.A., Gangopadhyay, A., de Castro, B.M., 2010. Eddy-induced upwelling off Cape São Tomé (22°S, Brazil). *Cont. Shelf Res.* 30 (10), 1181–1188.
- Campos, E.J.D., Gonçalves, J., Ikeda, Y., 1995. Water mass characteristics and geostrophic circulation in the South Brazil Bight: summer of 1991. *J. Geophys. Res.* 100, 18537–18550.
- Campos, E.J.D., Velhote, D., da Silveira, I.C.A., 2000. Shelfbreak upwelling driven by Brazil Current cyclonic meanders. *Geophys. Res. Lett.* 27 (6), 751–754.
- Castelão, M.R., 2012. Sea surface temperature and wind stress curl variability near a cape. *J. Phys. Oceanogr.* 42, 2073–2087.
- Castelão, M.R., Barth, J.A., 2006. Upwelling around Cabo Frio, Brazil: the importance of wind stress curl. *Geophys. Res. Lett.* 33, L03602. [10.1029/2005GL025182](http://dx.doi.org/10.1029/2005GL025182).
- Castelão, M.R., Campos, E.J.D., Miller, J.L., 2004. A modeling study of coastal upwelling driven by wind and meanders of the Brazil Current. *J. Coast. Res.* 20 (3), 662–671.
- Castro, B.M., Miranda, L.B., 1998. Physical Oceanography of the Western Atlantic continental shelf located between 4°N and 34°S coastal segment (4, W). In: Robinson, A.R., Brink, K.H. (Eds.), *The Sea: The Global Coastal Ocean - Regional Studies and Syntheses*. John Wiley & Sons, Inc., USA, pp. 209–251, vol. 11.
- Egbert, G.D., Erofeeva, S.Y., 2002. Efficient inverse modeling of barotropic ocean tides. *J. Atmos. Oceanic Technol.* 19 (2), 183–204.
- Emilson, I., 1961. The shelf and coastal waters off Southern Brazil. *Bol. Inst. Oceanogr.* 11 (2), 44–54.
- Evans, D., Signorini, S.R., 1985. Vertical structure of the Brazil Current. *Nature* 315, 48–50.
- França, G.B., Paes, R.C.O.V., Oliveira, A.N., Ruivo, B.C., Sartori, A., 2013. Daily blended microwave and infrared sea surface temperature composition. *Brazilian J. of Geophysics* 31 (2), 317–328.
- Gibbs, M., Middleton, J., Marchesiello, P., 1998. Barotropic response of Sidney shelf waters to local wind and deep ocean forcing. *J. Phys. Oceanogr.* 28 (2), 178–190.
- Haidvogel, D.B., Arango, H., Budgell, W.P., Cornuelle, B.D., Curchitser, E., Di Lorenzo, E., Fennel, K., Geyer, W.R., Hermann, A.J., Lanerolle, L., Levin, J., McWilliams, J.C., Miller, A.J., Moore, A.M., Powell, T.M., Shchepetkin, A.F., Sherwood, C.R., Signell, R.P., Warner, J.C., Wilkin, J., 2008. Ocean forecasting in terrain-following coordinates: formulations and skill assessment of the Regional Ocean Modeling System. *J. Comput. Phys.* 227, 3595–3624.
- Ikeda, Y., 1974. Observations on the stages of upwelling in the region of Cabo Frio (Brazil) as conducted by continuous surface temperature and salinity measurements. *Bol. Inst. Oceanogr.* 23, 33–46.
- Kanamitsu, M., Ebisuzaki, W., Woollen, J., Yang, S., Hnilo, J.J., Fiorino, M., Potter, G.L., 2002. NCEP/DOE AMIP-II Reanalysis (R-2). *BAMS* 83, 1631–1643.
- Kobayashi, S., Fujiwara, T., 2009. Modelling the long-term variability of shelf water intrusion into the Seto Inland Sea, Japan. *J. Marine Syst.* 77, 341–349.
- Kummerow, C., Barnes, W., Kozu, T., Shiue, J., Simpson, J., 1998. The tropical rainfall measuring mission (TRMM) sensor package. *J. Atmos. Oceanic Technol.* 15, 809–817.
- Lutjeharms, J.R.E., Cooper, J., Roberts, M., 2000. Upwelling at the inshore edge of the Agulhas Current. *Cont. Shelf Res.* 20, 737–761.
- MacCready, P., Rhines, P., 1993. Slippery bottom boundary layers on a slope. *J. Phys. Oceanogr.* 23, 5–22.
- Marta-Almeida, M., Pereira, J., Cirano, M., 2011. Development of a pilot Brazilian regional operational ocean forecast system, REMO-OOF. *J. Oper. Oceanogr.* 4 (2), 3–15.
- Mata, M.M., Cirano, M., vanCaspel, M.R., Fonteles, C.S., Goni, G., Baringer, M., 2012. Observations of Brazil Current baroclinic transport near 22°S: variability from the AX97 XBT transect. *Clivar Exchanges* 58 (17), 5–10.
- Oke, P.R., Middleton, J.H., 2001. Nutrient enrichment off Port Stephens: the role of the East Australian Current. *Cont. Shelf Res.* 21, 587–606.
- Oliveira, L.R., Piola, A.R., Mata, M.M., Soares, I.D., 2009. Brazil Current surface circulation and energetics observed from drifting buoys. *J. Geophys. Res.* 114, C10006. [10.1029/2008JC004900](http://dx.doi.org/10.1029/2008JC004900).
- Palma, E.D., Matano, R.P., 2009. Disentangling the upwelling mechanisms of South Brazil Bight. *Cont. Shelf Res.* 29, 1525–1534.
- Palma, E.D., Matano, R.P., Piola, A.R., 2008. A numerical study of Southwestern Atlantic Shelf circulation: stratified ocean response to local and offshore forcing. *J. Geophys. Res.* 113, C11010. [10.1029/2007JC004720](http://dx.doi.org/10.1029/2007JC004720).
- Palóczy, A., da Silveira, I.C.A., Castro, B.M., Calado, L., 2013. Coastal upwelling off Cape São Tomé (22°S, Brazil): the supporting role of deep ocean processes. *Cont. Shelf Res.* <http://dx.doi.org/10.1016/j.csr.2013.09.005>.
- Pereira, J., Cirano, M., Marta-Almeida, M., Amorim, F.N., 2013. A regional study of the Brazilian shelf/slope circulation (13°–31°S) using climatological open boundaries. *Brazilian J. of Geophys.* 31 (2), 289–305.
- Peterson, R.C., Stramma, L., 1991. Upper-level circulation in the south Atlantic Ocean. *Prog. Oceanogr.* 26, 1–73.
- Pickett, M.H., Paduan, J.D., 2003. Ekman transport and pumping in California Current based on the U.S. Navy's high resolution atmospheric model COAMPS. *J. Geophys. Res.* 108 (C10), 3327. [10.1029/2003JC001902](http://dx.doi.org/10.1029/2003JC001902).
- Richardson, P.L., Cheney, R.E., Worthington, L.V., 1978. A census of Gulf Stream rings Spring 1975. *J. Geophys. Res.* 83, 6136–6144.
- Rodrigues, R.R., Lorenzetti, J.A., 2001. A numerical study of the effects of bottom topography and coastline geometry on the southeast Brazilian coastal upwelling. *Cont. Shelf Res.* 21, 371–394.
- Rodrigues, R.R., Rothstein, L.M., Wimbush, M., 2007. Seasonal variability of the south equatorial bifurcation in the Atlantic ocean: a numerical study. *J. Phys. Oceanogr.* 37, 16–30.
- Roughan, M., Middleton, J.H., 2002. A comparison of observed upwelling mechanisms off the east coast of Australia. *Cont. Shelf Res.* 22, 2551–2572.
- Roughan, M., Middleton, J.H., 2004. On the East Australian Current: variability, encroachment and upwelling. *J. Geophys. Res.* 109, C07003. [10.1029/2003JC001833](http://dx.doi.org/10.1029/2003JC001833).
- Schmid, C.H., Schafer, H., Podesta, G., Zenk, W., 1995. The Vitoria Eddy and its relation to the Brazil Current. *J. Phys. Oceanogr.* 25 (11), 2532–2546.
- Shchepetkin, A.F., McWilliams, J.C., 2005. The regional ocean modeling system: a split-explicit, free-surface, topography following coordinates ocean model. *Ocean Modell.* 9, 347–404.
- Silveira, I.C.A., Schmidt, A.C.K., Campos, E.J.D., Godoi, S.S., Ikeda, Y., 2000. A corrente do Brasil ao largo da costa leste brasileira. *Rev. Bras. Oceanogr.* 48 (3), 171–183.
- Smith, R.L., 1968. Upwelling. *Oceanogr. Mar. Biol.* 6, 11–46.
- Smith, R.L., 1981. A comparison of the structure and variability of the flow field in three coastal upwelling regions: Oregon, North West Africa, and Peru. In: Robinson, F.A. (Ed.), *Coastal Upwelling*. American Geophysics Union, vol. 1, pp. 107–118.
- Soutelino, R.G.A., 2008. Origem da Corrente do Brasil. *Dissertação de Mestrado*, Instituto Oceanográfico, USP, São Paulo, Brasil, p. 120.
- Soutelino, R.G.A., daSilveira, I.C.A., Gangopadhyay, A., Miranda, J.A., 2011. Is the Brazil Current eddy-dominated to the north of 20°S? *Geophys. Res. Lett.* 38, L03607. [10.1029/2010GL046276](http://dx.doi.org/10.1029/2010GL046276).
- Stech, J.L., Lorenzetti, J.A., 1992. The response of South Brazil Bight to the passage of wintertime cold fronts. *J. Geophys. Res.* 97 (C6), 9507–9520.
- Stramma, L., England, M., 1999. On the water masses and mean circulation of the South Atlantic Ocean. *J. Geophys. Res.* 104 (C9), 20863–20883.
- Teixeira, C.E.P., Campos, E.J.D., Mata, M.M., Garcia, C.A.E., Lentini, C.A.D., 2009. On the temporal variability of the sea surface temperature in the southwestern Atlantic based on the analysis of Pathfinder AVHRR/NOAA images. *Revista Brasileira de Cartografia* 61 (3), 203–221.